Coherent control for selective excitation of combustion species in a benchtop flame using fs/ps CARS

Anna L. Stevenson* and Chloe E. Dedic†
University of Virginia, Charlottesville, VA 22903

Hybrid fs/ps coherent anti-Stokes Raman scattering employing coherent control is presented for selective excitation of combustion-relevant species. Femtosecond pulse shaping is accomplished experimentally using a 4-*f* pulse shaper with a spatial light modulator at the Fourier plane. A feedback-controlled genetic algorithm for adaptive pulse shaping is used to optimize for the selective excitation of CO_2 (near 1388 cm^{-1}) and O_2 (near 1556 cm^{-1}) rovibrational transitions in a non-reacting flow. 0D fs/ps CARS measurements acquired in a near-adiabatic flame demonstrate the use of coherent control in a combustion environment.

I. Introduction

The continued optimization of jet turbine engines is driven by a desire to increase fuel efficiency while minimizing pollutants that contribute to anthropogenic climate change. Aircraft exhaust emissions—which include carbon dioxide (CO_2), carbon monoxide, water vapor, nitrogen oxides (NOx), unburnt hydrocarbons (UHC), and particulate matter (PM)[1]—are responsible for approximately 3.5% of net anthropogenic effective radiative forcing [2]. Despite only accounting for approximately 3% of global CO_2 emissions [1], aviation emissions disproportionately impact climate as they emit directly into the sensitive upper troposphere and lower stratosphere, and alter a wide range of atmospheric processes [3]. Advances in sustainable fuels, propulsion technology, aircraft configuration, and low-emissions technology are required to mitigate the environmental impact of commercial transport aircraft [1]. While propulsion technology developments such as electric, hybrid, and hydrogen-powered aircraft have the potential for emission reduction, they also face numerous technical barriers making widespread adoption challenging in the near future. Sustainable aviation fuels (SAF) offer substantial advantages in CO_2, SO_2, and PM emissions when compared against conventional petroleum-based fuels, and do not require changes to existing engine or combustion chamber designs [4, 5]. However, the impact of SAF on unburnt hydrocarbon emissions is not well characterized. Differences in volatility, thermal stability, and viscosity between SAFs and traditional jet fuels can impact atomization and combustion performance, impacting NOx and UHC emissions [4]. High-fidelity hydrocarbon speciation is critical to understanding the impact of SAF on atmospheric chemistry processes and global climate change.

UHCs have the potential to impact atmospheric chemistry in a variety of ways. UHCs undergo photochemical reactions with NOx to produce ozone and secondary organic aerosols, which are primary contributors to photochemical smog and significantly impact air quality [4, 6]. As UHCs are emitted during all flight phases, they are dispersed into the atmosphere at all levels; causing for example both stratospheric ozone depletion as well as harmful tropospheric ozone production [1]. Despite their short atmospheric lifetime, UHCs are involved in a number of chemical reactions that can lead to the formation of greenhouse gases (i.e., methane and CO_2) and indirectly contribute to global warming [4]. UHCs are also directly related to condensable organics, which condense and agglomerate in the exhaust plume to form volatile particulate matter [7]. Measurements of individual chemical species that contribute to total UHC emissions are rare but are important for understanding the impact of different SAFs on both global climate and local air quality [8]. Speciation of total UHC emissions is important because different classes of organic molecules exhibit different environmental effects; for example, alkenes and aldehydes are the most reactive compounds for photochemical air pollution [9]. Even among the same class of hydrocarbons, different molecules may exhibit different behaviors. Therefore, individual hydrocarbon speciation is necessary to fully understand the impact of SAF emissions on atmospheric chemistry. For instance, among polycyclic aromatic hydrocarbons, anthracene ($C_{14}H_{10}$) and benzo[a]pyrene ($C_{20}H_{12}$) are the most reactive while fluoranthene ($C_{16}H_{10}$) and chrysene ($C_{18}H_{12}$) are the least reactive compounds towards ozone oxidation [10].

Hybrid femtosecond/picosecond coherent anti-Stokes Raman scattering (fs/ps CARS) allows for non-intrusive measurements of thermodynamic properties (i.e., species concentration, temperature, pressure) of combustion environments

*Graduate Research Assistant, Department of Mechanical and Aerospace Engineering, AIAA Student Member
†Assistant Professor, Department of Mechanical and Aerospace Engineering, AIAA Senior Member

with high spatial and temporal resolution [11–13]. Benefits of fs/ps CARS include kHz-scale measurement rates, high pulse energies, nonresonant background suppression, and relative insensitivity to collisions. fs CARS suffers from poor spectral resolution of neighboring pulses due to the bandwidth of the fs pulses. Relative to fs CARS, fs/ps CARS improves spectral resolution through the use of the ps probe pulse, which has a resolution of ~1-10 cm^{-1}. Studying UHC emissions, which may differ between various SAFs, with fs/ps CARS becomes difficult as the Raman fingerprint region (1000-1500 cm^{-1} [14]) may be quite congested when studying a complex mixture such as aircraft exhaust. As a result, selective excitation of molecular modes is being investigated using coherent control methods to improve the spectral sensitivity of fs/ps CARS for quantitative speciation of aircraft UHC emissions.

Quantum coherent control aims to direct a quantum system from an initial state to a final desired state through the exploitation of constructive and/or destructive quantum mechanical interferences [15, 16]. Coherent control of light interaction with matter can be accomplished with ultrafast laser pulse shaping through phase, amplitude, or polarization modulation [17], and can be applied to nonlinear optical spectroscopy methods to enhance a spectral feature of interest [18, 19]. For example, phase modulation of a CARS excitation pulse has been employed to achieve selective excitation of O_2 (1556 cm^{-1}) and N_2 (2230 cm^{-1}) vibrational modes in ambient air [20], N_2 (2330 cm^{-1}) and CO_2 (2230 cm^{-1}) vibrational modes in a 1:1 N_2/CO_2 mixture, [20], benzene (near 1050 cm^{-1}) and chloroform (near 700 cm^{-1}) vibrational modes in a binary liquid mixture [21], and individual vibrational modes (near 800, 1000, and 1200 cm^{-1}) of gas-phase toluene [22]. This work extends the use of coherent control with fs/ps CARS to a combustion environment. The use of phase modulation to achieve selective excitation of combustion reactant and product species in a hydrogen/air flame with CO_2 dilution is investigated. Q-branch transitions of O_2 (near 1556 cm^{-1}) and CO_2 (near 1280 and 1388 cm^{-1}) are targeted. Phase modulation is employed to selectively excite O_2 and CO_2 Q-branch transitions in a room-temperature gas jet and at elevated temperatures in a near-adiabatic benchtop flame. O_2 and CO_2 are targeted due to the relatively close spacing of their rovibrational transitions compared to previous studies. Additionally, as opposed to exhaust relevant hydrocarbons, the spacing of the rovibrational bands is large enough to allow for validation of the coherent control methods employed in this study.

II. Theory

A. Hybrid fs/ps CARS

Hybrid fs/ps CARS is a nonlinear, four-wave mixing spectroscopic technique that utilizes two fs pulses and one ps pulse overlapped spatially and temporally to produce a coherent laser-like signal containing thermodynamic information (i.e., temperature, pressure, species concentration) about the molecules in the overlapping probe volume. The two fs pump/Stokes pulses ($\omega_{pump}/\omega_{Stokes}$) provide high peak power broadband excitation of vibrational or rotational molecular transitions, and the ps probe pulse (ω_{probe}) is used to probe the molecular response. Frequency and timing diagrams for hybrid fs/ps CARS are shown in Fig. 1.

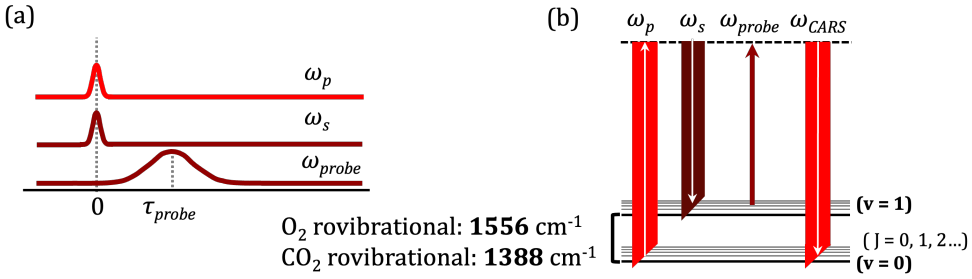

Fig. 1 (a) Timing and (b) and frequency diagrams for fs/ps CARS.

The CARS intensity $I_{CARS}(\omega)$ is proportional to the resonant and nonresonant third-order polarizations, $P^{(3)}_{res}(\omega)$ and $P^{(3)}_{nonres}(\omega)$, respectively [11]:

$$I_{CARS}(\omega) \propto |P^{(3)}_{res}(\omega) + P^{(3)}_{nonres}(\omega)|^2 \tag{1}$$

The nonresonant polarization can be neglected by delaying the probe pulse in time relative to the initial excitation. The

resonant polarization is dependent on the incoming electric fields of pump (E_p), Stokes (E_s), and probe (E_{pr}) and the CARS susceptibility (χ_{CARS}):

$$P^{(3)}_{res}(\omega_4) = \epsilon_0 \chi^{(3)}_{CARS}(\omega_4, \omega_1, \omega_2, \omega_3) E_p(\omega_1) E_s(\omega_2) E_{pr}(\omega_3) \tag{2}$$

The resonant frequency-domain polarization is the inverse Fourier transform of the induced time-domain complex polarization:

$$P^{(3)}_{res}(t) = \left(\frac{i}{\hbar}\right)^3 E_3(t) \int_0^\infty dt_2 \left[R_4(t_2) E_2^*(t + \tau_{23} - t_2) \times E_1(t + \tau_{23} + \tau_{12} - t_2) exp[i(\omega_1 - \omega_2)t]\right] \tag{3}$$

where τ_{12} is the delay between the pump and Stokes pulses, τ_{23} is the delay between the Stokes and probe pulses, $R_4(t)$ is the CARS molecular response, and ω_1 and ω_2 are the angular frequencies of the pump and Stokes pulses, respectively [23]. The excitation amplitude of the Raman mode induced by the interaction of pump and Stokes (with a frequency difference of Ω) is the convolution of the pump and Stokes electric fields: [19, 21]

$$A(\Omega) = E_s(\omega) \circledast E_p(\omega) = \int_0^\infty E_s^*(\omega - \Omega) E_p(\omega) d\omega = \int_0^\infty |E_s(\omega - \Omega) E_p(\omega)| e^{j[\psi(\omega) - \psi(\omega - \Omega)]} d\omega \tag{4}$$

where $\psi(\omega)$ is the spectral phase. Selective excitation of molecular modes can be achieved through phase modulation of one of the two excitation pulses; the Stokes pulse was modulated in this experiment. Q-branch transitions of O_2 (near 1556 cm^{-1}) and CO_2 (near 1280 and 1388 $^{-1}$) were targeted using the frequency difference between ω_{pump} and ω_{Stokes}. Feedback-controlled, closed-loop pulse shaping methods were employed to selectively excite the O_2 and CO_2 transitions individually.

B. Pulse Shaping

Femtosecond pulse shaping theory is based on the linear, time-invariant filter, which can be described in either the time or frequency domain [17]. In the time domain, the output of the pulse shaper is the convolution of the incoming electric field and an impulse response function which characterizes the pulse shaper:

$$e_{out}(t) = h(t) \circledast e_{in}(t) = \int dt' e_{in}(t') h(t - t') \tag{5}$$

Femtosecond pulse shaping is typically accomplished in the frequency domain, as electronics are not fast enough to allow for programmable control in the time domain. In the frequency domain, the resultant pulse is the product of the frequency response of the pulse shaper H(ω) and the incoming pulse:

$$E_{out}(\omega) = H(\omega) E_{in}(\omega) \tag{6}$$

where $e_{in}(t)$, $e_{out}(t)$, and $h(t)$ are Fourier transforms pairs of $E_{in}(\omega)$, $E_{out}(\omega)$, and $H(\omega)$ [17]. Pulse shaping is achieved experimentally using a 4-f pulse shaper, shown in Fig. 2, which consists of a pair of diffraction gratings and cylindrical lenses, and a pulse shaping mask at the Fourier plane. The first grating (G1) disperses the individual frequency components within the incident pulse, and the first lens (CL1) focuses them to small diffraction-limited spots at the Fourier plane. A mask is placed in this plane to manipulate the spatially dispersed optical Fourier components. Various 4-f configurations allow for control of phase [18, 20–22, 24, 25], amplitude [25], and/or polarization [24, 25]. This experiment utilizes phase masks created using a programmable liquid crystal on silicon spatial light modulator (LCoS SLM). SLMs utilize birefringent crystals to achieve user-specified phase shifts by modifying the optical path length of individual frequency components; a 2π phase shift changes the optical path length by approximately 1 wavelength. The mask acts both as a spatial and spectral mask, as spatial position and frequency are coupled at the Fourier plane; the field immediately after the SLM is described by Eq. 7:

$$E_m(x, \omega) = E_{in}(\omega) e^{-(x - \alpha\omega)^2 / w_0^2} M(x) \tag{7}$$

where α is the spatial dispersion at the masking plane, w_0 is the radius of the focused beam at the masking plane (for any single frequency component), and $M(x)$ is the masking function [17]. A second lens (CL2) and grating (G2) recombine frequencies into a collimated beam, and the shaped output pulse is the product of the Fourier transform of the mask

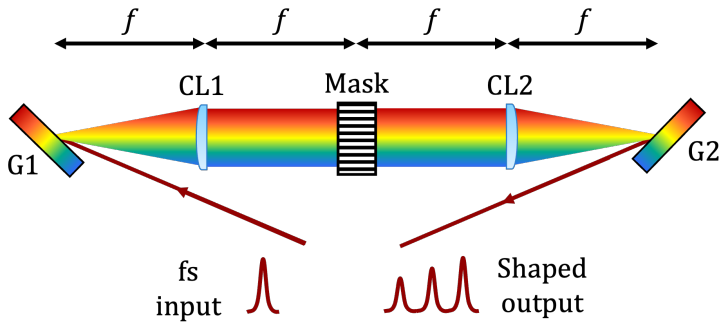

Fig. 2 4-*f* pulse shaper for fs pulse shaping with a transmissive mask.

and the input pulse. A pulse shaping mask with an appropriate transfer function can be designed if the desired output waveform is known by the user. However, in many real systems the appropriate laser waveform can be difficult to predict, especially for nonlinear processes where knowledge of the experimental Hamiltonian is insufficient [17, 26]. In these cases, adaptive pulse shaping using a feedback-controlled genetic algorithm is typically employed to search for the pulse waveform that gives the best experimental result according to a user-specified fitness function.

III. Methods and Experimental Setup

A. 4-*f* Pulse Shaper

The experimental reflective 4-*f* pulse shaper setup used in the current work is depicted in Fig. 3. The incoming amplified fs pulse (λ = 800 nm, Δt = 60 fs, 1 kHz) was directed to a holographic grating (Spectrogon, 1200 lines/mm, efficiency ≥90% at 800 nm) which dispersed the individual frequency components. A cylindrical lens (f = 250 mm) imaged the frequency components onto a reflective LCoS-SLM (Santec SLM-300) at the Fourier plane. A half waveplate was used to match the optical axis of the SLM crystals.

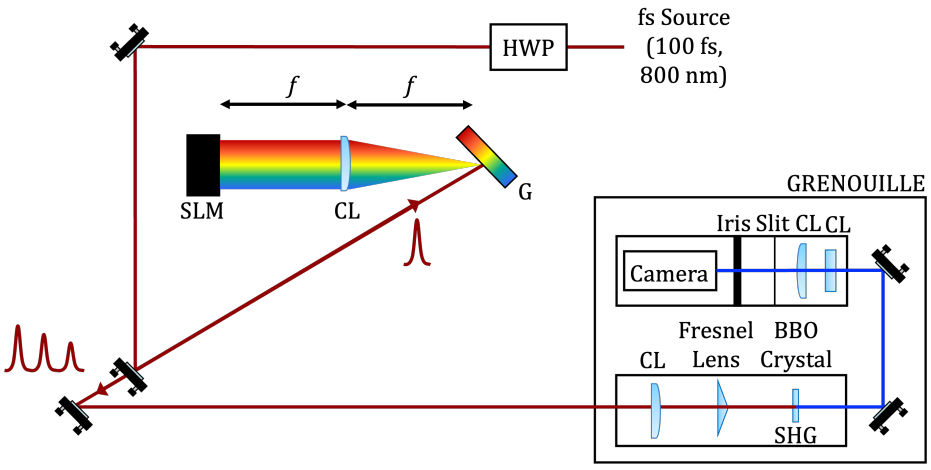

Fig. 3 4-*f* pulse shaper for fs pulse shaping with a programmable phase mask at the Fourier plane. HWP: half waveplate; G: grating; CL: cylindrical lens; SLM: spatial light modulator; BBO: beta barium borate; SHG: second harmonic generation; GRENOUILLE: grating-eliminated no-nonsense observation of ultrafast incident laser light e-fields.

Prior to CARS measurements, the recombined pulse was characterized using a simplified second harmonic generation (SHG) frequency-resolved optical gating (FROG) setup referred to as grating-eliminated no-nonsense observation of ultrafast incident laser light e-fields (GRENOUILLE) [27]. Also shown in Fig. 3, the incoming pulse was split into

two equal components using a Fresnel lens and overlapped in a thick beta barium borate (BBO) crystal; the SHG emission was directed to a CMOS camera (Teledyne Flir Blackfly S USB3). The resulting signal at the camera is a GRENOUILLE trace with delay along the x-axis and wavelength along the y-axis. These GRENOUILLE traces can be analyzed using the Trebino-Group SHG FROG code [28], which yields a reconstructed trace, the pulse intensity, phase, spectrum, and spectral phase.

B. CARS

The experimental fs/ps CARS setup is depicted in Fig. 4. A 1-kHz, Ti:sapphire laser (Coherent Astrella) produces a fs pulse (λ = 800 nm, Δt = 60 fs) which was split after pulse amplification. One portion was directed to a pulse compressor followed by an optical parametric amplifier (Light Conversion TOPAS-Prime) which was used to generate a frequency-tunable pump pulse. In this experiment, the pump wavelength was tuned to 710 nm to detect Q-branch transitions of O_2 (near 1556 cm^{-1}) and CO_2 (near 1280 and 1388 cm^{-1}) simultaneously. The second portion of the amplified fs pulse was directed to a pulse compressor and split again. One portion served as the Stokes pulse and was directed through the 4-f pulse shaper described in Section III.A to produce a "shaped" excitation pulse. The Stokes pulse was phase modulated to achieve selective excitation of the individual CO_2 and O_2 transitions. The other portion was directed to a second 4-f pulse shaper (1200 lines/mm holographic grating, 250 mm cylindrical lens) with a slit at the Fourier plane to generate a narrowband probe pulse (λ = 800 nm, δt = 5 ps). The pump and probe beamlines included delay stages to ensure temporal overlap. The probe delay was set to 5.2 ps to suppress nonresonant background. The per-pulse energies of the pump, Stokes, and probe beams measured before the probe volume were 56 μJ, 560 μJ, and 11 μJ, respectively. The three beams were focused at the probe volume using a single 250 mm lens, and the outgoing CARS signal was collimated with a 200 mm lens. A folded BOXCARS phase-matching configuration with a crossing angle of 4° was employed to satisfy the conservation of momentum and enable spectral filtering of the CARS signal. The generated CARS signal was focused into a 0.32 m spectrometer with a 2400 line/mm grating (IsoPlane 320, Princeton Instruments) and spectra were recorded using an electron-multiplied charge-coupled device (EMCCD) camera (ProEM 1600 eXcelon 3).

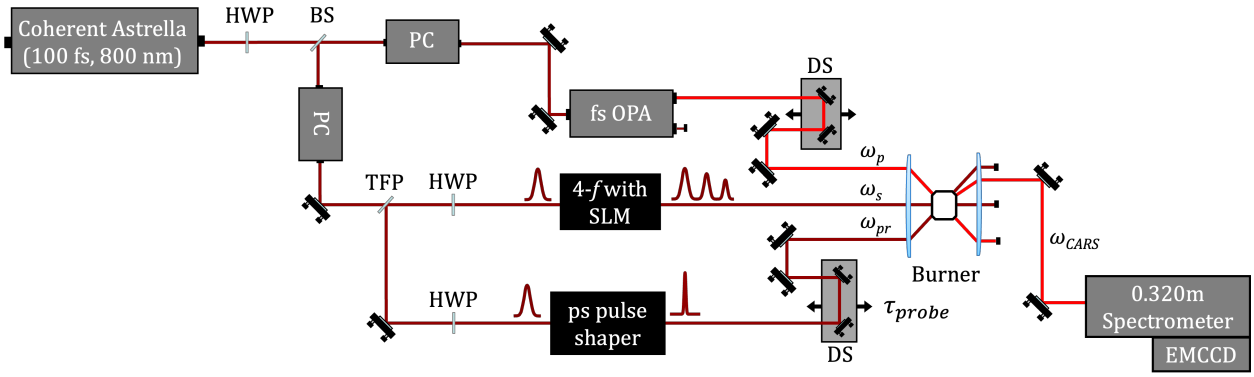

Fig. 4 Experimental fs/ps CARS schematic. HWP: half waveplate, BS: beam splitter, PC: pulse compressor; DS: delay stage; TFP: thin film polarizer; OPA: optical parametric amplifier; SLM: spatial light modulator; EMCCD: electron-multiplied charge-coupled device camera.

C. Genetic Algorithm

A feedback-controlled genetic algorithm was used to search for the pulse waveform that yields the best experimental result according to a user-specified fitness function. In this experiment, the selective excitation of CO_2 and O_2 rovibrational transitions was desired. For the selective excitation of CO_2, the GA attempted to improve the excitation of the CO_2 rovibrational band near 1388 cm^{-1} by suppressing the O_2 rovibrational band near 1556 cm^{-1}; the opposite occurred for the selective excitation of O_2. The algorithm started with a randomly generated population of individuals, which are the phase masks applied to the SLM. CARS spectra were acquired for each individual in the population. A fitness value was calculated for each individual according to a goal defined by the user. The individuals were then ranked in terms of fitness; each iteration retained the best performing 40% of individuals. The remaining 60% of individuals

were generated through a crossover and mutation process. In this study, the population size was 30, the crossover rate was 0.25, and the mutation rate was 0.5. The algorithm would run until the best fitness calculated was 0—indicating that the experimental CARS spectrum matched the goal output—but quit early if the same individual is selected was "best" for more than 5 iterations in a row, or if 25 iterations were completed. To test the functionality of the GA, the individuals were limited to slit masks. The GA controls the width and center location of the slit; the phase shift of the slit was set at 0 and all other pixels were set to a phase shift of π. To define a goal output, a CARS spectrum with no phase mask applied was acquired; specific pixel ranges in the frequency axis were selected for frequency elimination. For each individual in a population, 1000 spectra were acquired with an exposure time of 0.1 ms; these spectra were background subtracted and averaged before being compared against the goal output. An individual's fitness was calculated using the sum of squares between the goal and the individual's normalized spectra, denoted as $\tilde{I}$ and $\tilde{G}$ in Eq. 8, respectively. Different weighting functions can be defined based on which frequencies should contribute more significantly to the the GA result.

$$fitness = \sum \sqrt{weight\left(\tilde{I} - \tilde{G}\right)} \tag{8}$$

D. Combustion System

A non-premixed Hencken burner was used to generate a near-adiabatic H_2 flame. The Hencken burner consists of a 600 mm^2 honeycomb burner surface surrounded by a 844 mm^2 coflow. Stainless steel fuel tubes are nested inside the honeycomb structure and distributed evenly; each fuel tube is surrounded by six oxidizer tubes. When operating under non-premixed conditions, the fuel and oxidizer flow out of their respective tubes and a series of small diffusion flames are stabilized above the burner surface. For this experiment, the equivalence ratio was fixed at 0.3; the corresponding flow rates of air, H_2, and N_2 coflow were 55 SLPM, 6.9 SLPM, and 85 SLPM, respectively. CO_2 was seeded into the air input of the burner; the mole fraction of CO_2 in the reactants was set at 7%. CARS measurements were acquired at a height of 3 mm above the burner surface, within a region where uniform temperature near the adiabatic flame temperature is expected [29]. Room temperature CARS spectra of CO_2 and O_2 were acquired by flowing CO_2 and air through the burner oxidizer tubes at flow rates of 8 and 10 SLPM, respectively.

IV. Results

A. Selective excitation via feedback controlled, closed-loop femtosecond pulse shaping

Femtosecond pulse shaping capability was initially demonstrated using a 4-f pulse shaper with an SLM at the Fourier plane. Four different phase masks are shown in the top row of Fig. 5 including: a slit mask, where a phase shift of π has been applied to the center 10% of pixels and a constant phase shift of 0 has been applied to the rest of the SLM; a sine mask, with an amplitude of 2π and a period of 65 pixels (5% of SLM width); a step mask, where a constant phase shift of π has been applied to the left half of the SLM, and a constant phase shift of 0 has been applied to the right half; a linear mask, where a linear phase shift from 0 to π has been applied to the left half of the SLM, and a constant phase shift of 0 has been applied to the right half. Experimental GRENOUILLE traces corresponding to each mask are shown in the second row of Fig. 5; a GRENOUILLE trace corresponding to a constant phase shift of 0 has also been included for reference. The Trebino SHG FROG code was used to generate the reconstructed traces with G-errors [30] less than 1%. Pulse intensity and phase, and the pulse spectrum and spectral phase were extracted from the reconstructed traces.

Feedback controlled, closed-loop femtosecond pulse shaping using a genetic algorithm (GA) is utilized to achieve selective excitation of CO_2 and O_2 rovibrational transitions in the Hencken burner flame. For the selective excitation of CO_2, the GA tries to improve the excitation of the CO_2 rovibrational band near 1388 cm^{-1} while suppressing the O_2 rovibrational band near 1556 cm^{-1}; the opposite occurs for the selective excitation of O_2. The algorithm was used to generate two masks: one to optimize for the suppression of the CO_2 band near 1388 cm^{-1} and the other to optimize for the suppression of the O_2 band near 1556 cm^{-1}. The optimization routine utilized CARS spectra acquired at room temperature in a non-reacting gas jet for feedback. Room-temperature spectra rather than high-temperature exhaust gases were used for two reasons: (1) to achieve high signal-to-noise ratios for testing the algorithm and (2) because of the long times currently required for the GA to converge upon an optimal phase mask. Additionally, running the GA in a non-reacting flow such as a gas jet is desirable for the detection of UHCs. As the composition of aviation exhaust may not be known, optimal phase masks for individual hydrocarbons should be designed using a mixture of known gases and then applied to a combustion environment for hydrocarbon speciation.

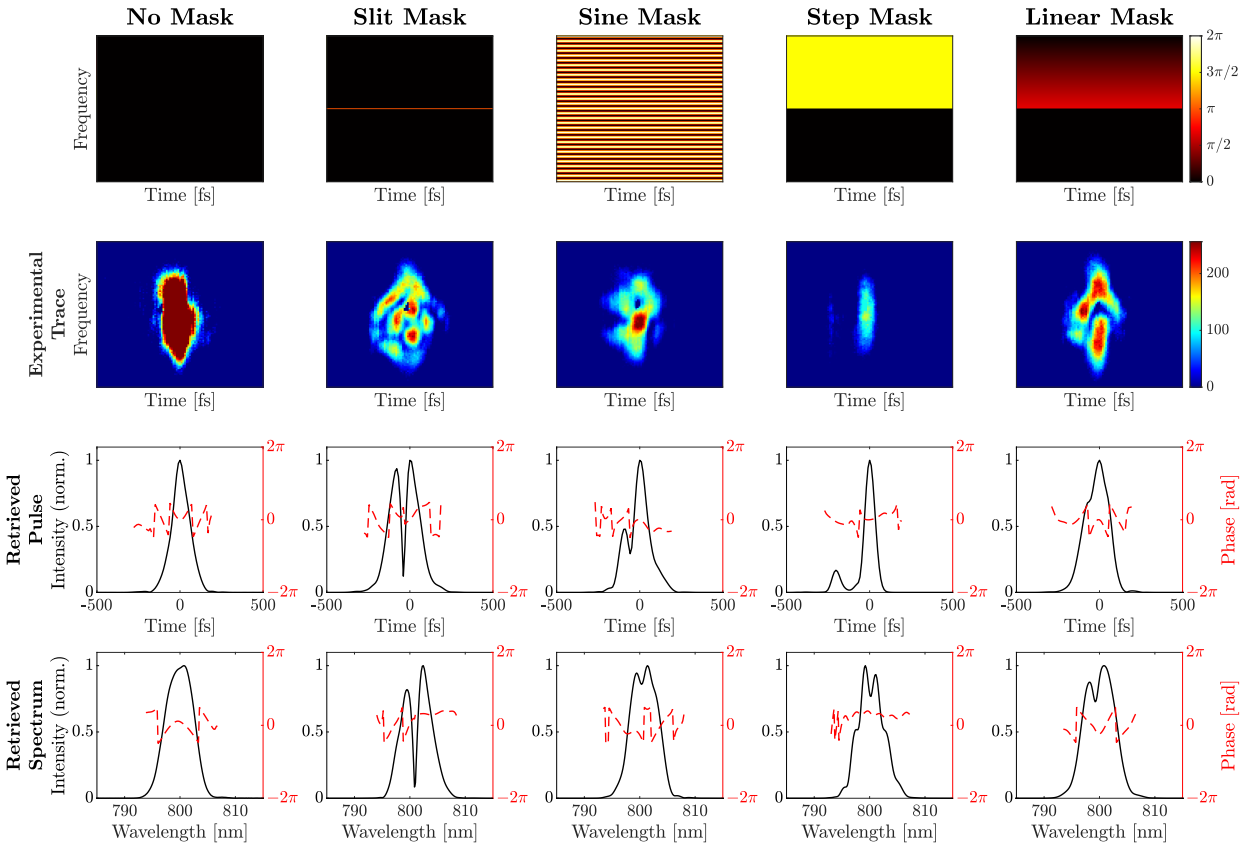

Fig. 5 Various phase masks for fs pulse shaping (1st row); corresponding experimental GRENOUILLE traces (2nd row); SHG FROG traces retrieved using Trebino FROG algorithm (3rd row); the retrieved pulse in the time (4th row) and frequency (5th row) domains.

CARS spectra were acquired in a near-adiabatic H_2 flame with and without the phase mask selected by the genetic algorithm for suppression of the CO_2 rovibrational band. The results for the selective excitation of O_2 near 1556 cm^{-1}, relative to CO_2 near 1388 cm^{-1}, are shown in Fig. 6. In both cases, 3000 CARS spectra were acquired with an exposure time of 25 ms. Spectra were background subtracted and then averaged; results are shown in Fig. 6. The spectra are normalized to the oxygen peak around 1556 cm^{-1}. The average maximum intensities recorded on the 16-bit sensor with and without the phase mask were 4,477 and 10,460, respectively. The optimal phase mask selected by the GA had a slit width of 359 pixels (30% of SLM width) and was centered at pixel 1227. As shown in Fig. 6, the intensity of the CO_2 band near 1388 cm^{-1} has been clearly suppressed relative to the O_2 band. Without the phase mask, the normalized peak intensity of CO_2 relative to O_2 was 1.985. With the phase mask applied, the normalized intensity of CO_2 was 0.348, resulting in a suppression factor of 82.5% relative to O_2. The intensity of the CO_2 band at 1388 cm^{-1} relative to the CO_2 band at 1280 cm^{-1} was 3.38:1 without the mask, and 2.96:1 with the phase mask, indicating that the 1388 cm^{-1} band has also been suppressed relative to the 1280 cm^{-1} band. However, full suppression of the CO_2 band was not observed. The algorithm terminated optimization before reaching convergence because it had already performed 25 iterations.

CARS spectra were acquired with and without the phase mask designed by the genetic algorithm for the suppression of the O_2 rovibrational band. The results for the selective excitation of the CO_2 rovibrational band near 1338 cm^{-1}, relative to O_2 near 1556 cm^{-1}, are shown in Fig. 7. In both cases, 3000 CARS spectra were acquired with an exposure time of 25 ms. Spectra were background subtracted and then averaged; results are shown in Fig. 6. The spectra are normalized to the peak CO_2 intensity around 1388 cm^{-1}. The optimal phase mask designed by the GA had a slit width of 248 pixels (21% of SLM width) and a center location of 1546. The average maximum intensity with the phase mask was 4,805. Nonresonant contribution is observed in Fig. 6 and can be suppressed in the future through a more optimal selection of probe delay. It can be seen in Fig. 6 that the intensity of the O_2 band near 1556 cm^{-1} has been slightly suppressed relative to the CO_2 band near 1388 cm^{-1}. Without the phase mask, the intensity of the O_2 feature

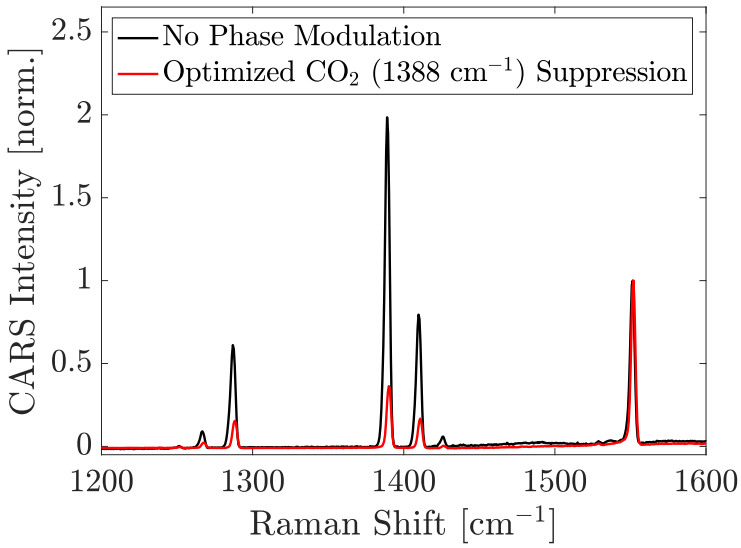

Fig. 6 Experimental CARS spectra of CO_2 and O_2 in a H_2 flame with and without a phase mask optimized for the selective excitation of the O_2 peak near 1556 cm^{-1} (and suppression of the CO_2 band near 1388 cm^{-1}).

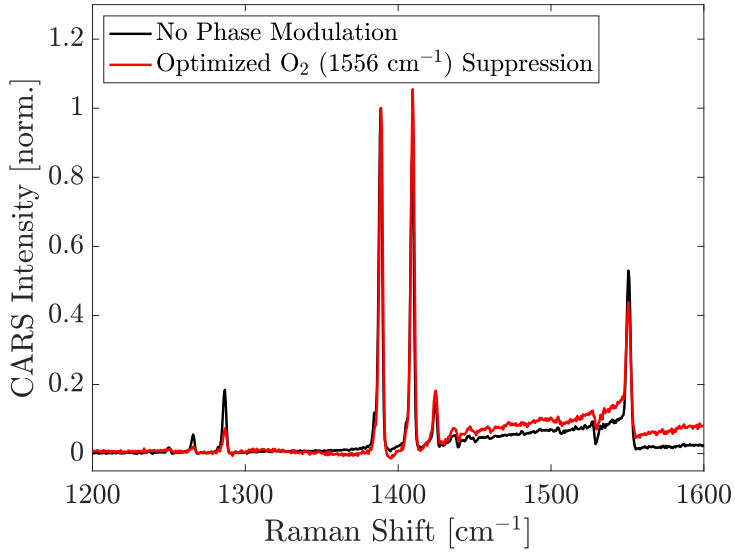

Fig. 7 Experimental CARS spectra of CO_2 and O_2 in a H_2 flame with and without a phase mask optimized for the selective excitation of the CO_2 peak near 1388 cm^{-1} (and suppression of the O_2 band near 1556 cm^{-1}).

normalized relative to CO_2 was 0.529. With the phase mask applied, the normalized intensity of O_2 was 0.438, resulting in a suppression factor of 17% relative to CO_2. The intensity of the CO_2 band at 1388 cm^{-1} relative to the CO_2 band at 1280 cm^{-1} was 5.417:1 without the mask, and 13.69:1 with the phase mask, indicating that the 1280 cm^{-1} band has been suppressed relative to the 1388 cm^{-1} band. Once again, the algorithm terminated optimization before reaching convergence because it had already performed 25 iterations. The mask selected by the genetic algorithm for the selective excitation of CO_2 is not optimal, as a suppression factor close to 100% is desired. Further investigation into algorithm parameters is necessary to improve selective excitation.

The optimization speed and final result depend strongly on the number of parameters the GA can control [31]. In this case, the GA was able to control 1920 parameters for the location of the slit, and 500 parameters for the slit width. Decreasing the number of parameters the GA is able to select, particularly for slit location, could aid in optimization

speed and convergence. Modifications to GA parameters such as population size, crossover rate, and mutation rate may also improve the final result; for example, a lower mutation rate would likely improve convergence [31]. Modifications to the fitness function, such as only considering ratios of different rovibrational bands instead of the entire spectrum, may also improve selective excitation [21]. Allowing the algorithm to consider mask types other than slit masks, such as sinusoidal, polynomial, or pseudorandom binary masks, may also improve the final result.

B. Improved selective excitation via manual phase mask application

Ideally, the genetic algorithm should identify the phase mask that is optimal for the selective excitation of a desired rovibrational transition. However, it is evident from the CO_2 selective excitation results shown in Fig. 7 that further development of the GA is needed to improve the optimization process. Various phase masks were generated and applied manually to test if improved suppression of a rovibrational band could be obtained without the GA. Slit masks with a slit width and center location of 100 and 1200 pixels, respectively, were generated and applied. The phase shift applied to the slit was varied from 0 to 2π; the background pixels were fixed at a phase shift of 0π. 1000 room temperature CARS spectra were acquired at an exposure time of 0.1 ms, background subtracted, and averaged. Selected results are shown in Fig. 8, focusing on the suppression observed for the CO_2 band near 1388 cm^{-1}. For this result, the pump wavelength was tuned to 718 nm to enhance the excitation of the CO_2 Q-branch transitions. It can be seen in Fig. 8 that the phase shift applied to the slit mask impacts the degree of suppression for various rovibrational transitions within the CO_2 band. Phase shifts of π were applied to the slit masks generated by the genetic algorithm, but a phase shift of 0.7π appears more effective at suppressing the transitions around 1388 cm^{-1}. Allowing the genetic algorithm to control not only the width and center location of the slit, but the phase applied as well, would likely improve the effectiveness of the resulting mask.

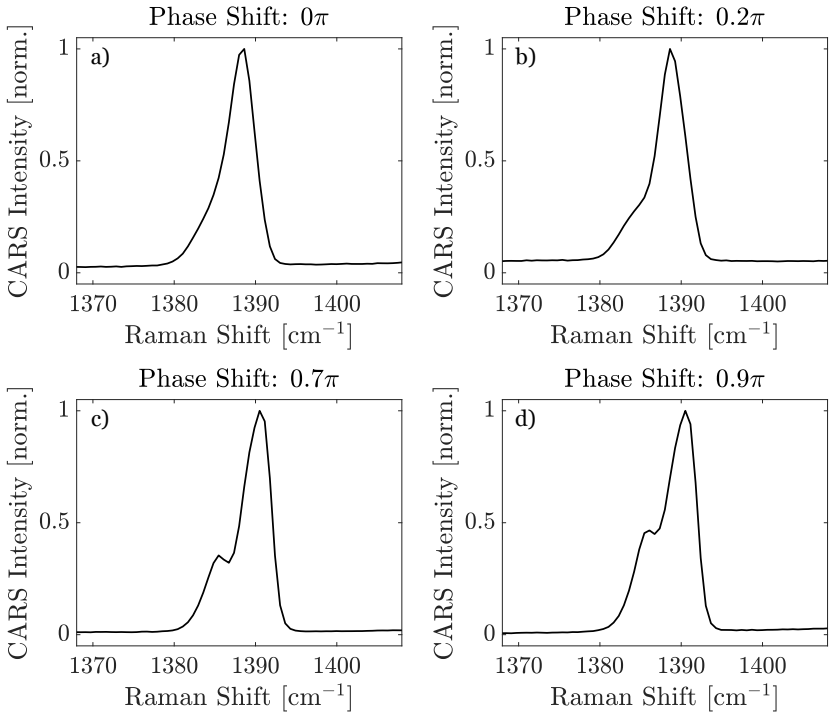

Fig. 8 Room temperature experimental CARS spectra of the CO_2 rovibrational band near 1388 cm^{-1} with phase shifts of a) 0π, b) 0.2π, c) 0.7π, and d) 1π applied to a slit mask (width and center location of 100 and 1200 pixels, respectively).

In addition to investigating the impact of phase shift on selective excitation, the impact of pump/Stokes timing overlap was also studied. A slit mask with a slit width and center location of 100 and 1200, respectively, and a center phase shift of π was applied. The pump delay stage was adjusted in increments of 10 fs. At each delay, 1000 room

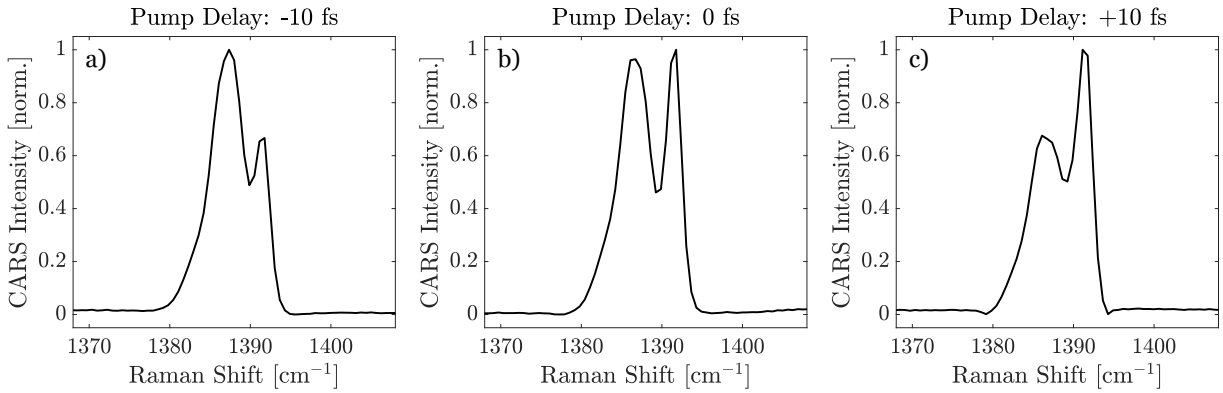

Fig. 9 Room temperature experimental CARS spectra of the CO_2 rovibrational band near 1388 cm^{-1} with a constant slit mask applied (phase shift, background, width, and center location of π, 0π, 100, and 1200 pixels, respectively) and pump delays of a) -10 fs, b) 0 fs, and c) +10 fs.

temperature CARS spectra were acquired at an exposure time of 0.1 ms, background subtracted, and averaged; selected results are shown in Fig. 9. Pump delay has been centered around Fig. 9B where it can be seen that certain frequencies within the CO_2 rovibrational band have been suppressed around 1388 cm^{-1}. When pump delay is set at -10 fs, transitions within the rovibrational band centered around 1391 cm^{-1} are suppressed. When pump delay is set at +10 fs, transitions within the rovibrational band centered around 1386 cm^{-1} are suppressed. This behavior with variable pump delay was not observed when no phase mask was applied. These results clearly demonstrate the capability to suppress specific transitions within a rovibrational band.

As described previously by Equation 4, the excitation amplitude of the Raman mode is determined by the interference between all frequency pairs within the pump and Stokes excitation pulses separated by Ω. The contribution of different two-photon pairs interfere with a relative phase $\phi(\omega) - \phi(\omega - \Omega)$ [18]. As the relative timing overlap between pump and Stokes changes, the frequency that has been phase-shifted using the SLM interacts with different frequencies in the pump bandwidth, impacting the two-photon interaction process. This results in interference that manifests as different transitions within the rovibrational band being suppressed. The ability to suppress these individual transitions with manually applied masks indicates that improved selective excitation/suppression of combustion species is possible in the future after implementing improvements including modifications to the evolutionary algorithm.

V. Summary and Future Work

The use of coherent control with fs/ps CARS for selective excitation of combustion species in a near-adiabatic flame has been demonstrated. A genetic algorithm was used to select optimal phase masks for the selective excitation of spectral bands of CO_2 near 1388 cm^{-1} and O_2 near 1556 cm^{-1}. The masks produced by the GA yielded a suppression factor of 82.5% for CO_2 relative to O_2, and 17% for O_2 relative to CO_2. A suppression factor of 100% is desired. While the basic functionality of the GA has been demonstrated through CO_2 suppression, the optimization routine currently struggles to suppress relatively low energy transitions, as demonstrated by the lack of O_2 suppression. Modifications to algorithm parameters including population size, crossover and mutation rates, the fitness function, and controllable parameters will all be explored to improve its functionality. Control of various types of phase masks (i.e., sinusoidal, pseudorandom binary) as well as control over the phase applied to slit masks will be explored in the future. The ability to suppress transitions within a single rovibrational band through small changes in pump/Stokes temporal overlap has also been demonstrated. The ability to suppress these transitions through a manually applied mask indicates that enhanced selective excitation is possible in the future. Modifications to the fs/ps CARS system will be explored for increased suppression of rovibrational transitions. In the future, this technique will be extended to studying neighboring Raman transitions and hydrocarbon mixtures relevant to aviation exhaust. Additionally, coherent control for improving dynamic range through the suppression of strong rovibration bands will be investigated in order to detect low-concentration UHCs.

Acknowledgments

This work was supported by the National Science Foundation Award #2033675. A. Stevenson was supported by the University of Virginia Rolls Royce Fellowship and the National Science Foundation Graduate Research Fellowship. The authors also thank Sean Sawaya, Laurie Elkowitz, Madalyn Yates, Taka Suzuki, and Michael Novak at the University of Virginia Reacting Flow Laboratory for experimental assistance.

References

[1] Ranasinghe, K., Guan, K., Gardi, A., and Sabatini, R., "Review of advanced low-emission technologies for sustainable aviation," *Energy*, 2019.

[2] Gossling, S., and Lyle, C., "Transition policies for climatically sustainable aviation," *Transport Reviews*, 2021. https://doi.org/https://doi.org/10.1080/01441647.2021.1938284.

[3] Schumann, U., "On the effect of emissions from aircraft engines on the state of the atmosphere," *Annales Geophysicae*, 1994.

[4] Song, Z., Li, Z., and Lui, Z., "Comparison of Emission Properties of Sustainable Aviation Fuels and Conventional Aviation Fuels: A Review," *Applied Sciences*, 2024. https://doi.org/10.3390/app14135484.

[5] Wang, B., Ting, Z., and Zhao, M., "Sustainable aviation fuels: Key opportunities and challenges in lowering carbon emissions for aviation industry," *Carbon Capture Science and Technology*, 2024. https://doi.org/10.1016/j.ccst.2024.100263.

[6] Gao, Y., Li, M., Wan, X., Zhap, X., Wu, Y., Liu, X., and Li, X., "Important contributions of alkenes and aromatics to VOCs emissions, chemistry and secondary pollutants formation at an industrial site of central eastern China," *Atmospheric Environment*, 2021. https://doi.org/10.1016/j.atmosenv.2020.117927.

[7] Owen, B., Anet, J., Bertier, N., Christie, S., Cremaschi, M., Dellaert, S., Edebeli, J., Janicke, U., Kuenen, J., Lim, L., and Terrenoire, E., "Review: Particulate Matter Emissions from Aircraft," *Atmosphere*, 2022. https://doi.org/10.3390/atmos13081230.

[8] Yelvington, P., Herndon, S., Wormhoudt, J., Jayne, J., Miake-Lye, R., Knighton, W., and Wey, C., "Chemical Speciation of Hydrocarbon Emissions from a Commercial Aircraft Engine," *Journal of Propulsion and Power*, 2007. https://doi.org/10.2514/1.23520.

[9] Spicer, C. W., Holdren, M. W., Smith, D. L., Hughes, D. P., and Smith, M. D., "Chemical composition of exhaust from aircraft turbine engines," *ournal of Engineering for Gas Turbines and Power*, 1992. https://doi.org/https://doi.org/10.1115/1.2906292.

[10] Perraudin, E., Budzinski, H., and Villenave, E., "Kinetic Study of the Reactions of Ozone with Polycyclic Aromatic Hydrocarbons Adsorbed on Atmospheric Model Particles," *Journal of Atmospheric Chemistry*, 2007. https://doi.org/10.1007/s10874-006-9042-x.

[11] Dedic, C. E., "Hybrid fs/ps coherent anti-Stokes Raman scattering for multiparameter measurements of combustion and nonequilibrium," *Doctoral Thesis, Iowa State University*, 2017.

[12] Miller, J. D., Slipchenko, M. N., Meyer, T. R., U., S. H., and Gord, J. R., "Hybrid femtosecond/picosecond coherent anti-Stokes Raman scattering for high-speed gas-phase thermometry," *Optics Letters*, 2010. https://doi.org/10.1364/OL.35.002430.

[13] Kearney, S. P., "Hybrid fs/ps rotational cars temperature and oxygen measurements in the product gases of canonical flat flames," *Combustion and Flame*, 2015. https://doi.org/10.1016/j.combustflame.2014.11.036.

[14] Dudovich, N., Oron, D., and Silberberg, Y., "Single-pulse coherent anti-Stokes Raman spectroscopy in the fingerprint spectral region," *Journal of Physical Chemistry*, 2003. https://doi.org/10.1063/1.1568072.

[15] Oron, D., Dudovich, N., Yelin, D., and Silberbger, Y., "Quantum control of coherent anti-Stokes Raman processes," *Physical Review A*, 2002. https://doi.org/10.1103/PhysRevA.65.043408.

[16] Silberberg, Y., "Quantum Coherent Control for Nonlinear Spectroscopy and Microscopy," *Annual Review of Physical Chemistry*, 2009. https://doi.org/10.1146/annurev.physchem.040808.090427.

[17] Weiner, A., "Femtosecond pulse shaping using spatial light modulators," *Review of Scientific Instruments*, 2000. https://doi.org/10.1063/1.1150614.

[18] Dudovich, N., Oron, D., and Silberberg, Y., "Single-pulse coherently controlled nonlinear Raman spectroscopy and microscopy," *Nature*, Vol. 48, 2002.

[19] Weiner, A., "Ultrafast Optical Pulse Shaping: A Tutorial Review," *Optics Communications*, 2011. https://doi.org/10.1016/j.optcom.2011.03.084.

[20] Wrzesinski, P. J., Pestov, D., Lozovoy, V. V., Xu, B., Roy, S., Gord, J. R., and Dantusa, M., "Binary phase shaping for selective single-beam CARS spectroscopy and imaging of gas-phasemolecules," *Journal of Raman Spectroscopy*, 2010. https://doi.org/10.1002/jrs.2709.

[21] Konradi, J., Singh, A. K., and Materny, A., "Selective excitation of molecular modes in a mixture by optimal control of electronically nonresonant femtosecond four-wave mixing spectroscopy," *Journal of Photochemistry and Photobiology A: Chemistry*, 2006. https://doi.org/10.1016/j.jphotochem.2006.02.009.

[22] Scaria, A., Konradi, J., Namboodiri, V., and Materny, A., "A comparison of the selective excitation of molecular modes in gas and liquid phase using femtosecond pulse shaping," *Journal of Raman Spectroscopy*, 2008. https://doi.org/10.1002/jrs.1967.

[23] Stauffer, H., Miller, J., Slipchenko, M., Meyer, T., Prince, B., Roy, S., and Gord, J., "Time- and frequency-dependent model of time-resolved coherent anti-Stokes Raman scattering (CARS) with a picosecond-duration probe pulse," *Journal of Chemical Physics*, 2014. https://doi.org/10.1063/1.4860475.

[24] Lim, S., Caster, A., Nicolet, O., and Leone, S., "Chemical Imaging by Single Pulse Interferometric Coherent Anti-Stokes Raman Scattering Microscopy," *Journal of Physical Chemistry B*, 2006. https://doi.org/10.1021/jp057493k.

[25] Wefers, M., and Nelson, K., "Generation of high-fidelity programmable ultrafast optical waveforms," *Optics Letters*, 1995. https://doi.org/10.1364/ol.20.001047.

[26] Baumert, T., Brixney, T., Seyfried, V., Strehle, M., and Gerber, G., "Femtosecond pulse shaping by an evolutionary algorithm with feedback," *Applied Physics B*, 1997.

[27] O'Shea, P., Kimmel, M., Gu, X., and Trebino, R., "Highly simplified device for ultrashort-pulse measurement," *Optics Letters*, 2001. https://doi.org/10.1364/OL.26.000932.

[28] Trebino, R., "Trebino-Group FROG Code," *Accessed online*, https://frog.gatech.edu/code.html.

[29] Hancock, R., Bertagnolli, K., and Lucht, R., "Nitrogen and hydrogen CARS temperature measurements in a hydrogen/air flame using a near-adiabatic flat-flame burner," *Combustion and Flame*, 1997. https://doi.org/10.1016/S0010-2180(96)00191-5.

[30] Xu, L., Zeek, E., and Trebino, R., "Simulations of frequency-resolved optical gating for measuring very complex pulses," *Journal of the Optical Society of America B*, 2008.

[31] Ziedler, D., Frey, S., Kompa, K., and Motzkus, M., "Evolutionary algorithms and their application to optimal control studies," *Physical Review A*, 2001. https://doi.org/10.1103/PhysRevA.64.023420.